

Cite this: *J. Mater. Chem. A*, 2019, 7, 8845

Oxygen loss and surface degradation during electrochemical cycling of lithium-ion battery cathode material LiMn_2O_4 †

HPSTAR
898-2019Xiang Gao, ^{‡a} Yumi H. Ikuhara, ^a Craig A. J. Fisher, ^{*,a} Rong Huang, ^b Akihide Kuwabara, ^a Hiroki Moriwake, ^a Keiichi Kohama^c and Yuichi Ikuhara ^{*,ad}

Electrode surfaces play a critical role in determining the electrochemical performance of lithium-ion batteries, and uncovering how surface chemistry and structure evolve during cycling, particularly at the atomic level, is necessary for improved battery materials design. We report a scanning transmission electron microscopy (STEM) investigation into the atomistic mechanisms behind surface reconstruction induced by electrochemical cycling of cathode material LiMn_2O_4 . Direct STEM observations reveal that surface layers of as-synthesised LiMn_2O_4 thin films are subject to considerable compressive lattice strain as a result of oxygen deficiency. During the first charge, the lattice strain increases significantly, resulting in a reconstruction reaction to form Mn_3O_4 with further loss of oxygen from the topmost layers. Continued cycling leads to deterioration of surface crystallinity. The observed irreversible structure changes affect charge transfer reaction kinetics at LiMn_2O_4 surfaces because Li pathways become blocked by Mn atoms, contributing to a reduction in long-term cycle life and energy capacity. The ability to observe atomic-level changes at electrode surfaces at different stages of cycling provides a more robust understanding of electrode processes that can accelerate development of safer and longer-lasting battery materials.

Received 20th August 2018
Accepted 27th November 2018

DOI: 10.1039/c8ta08083f

rsc.li/materials-a

1. Introduction

The important role of materials interfaces (esp. electrode/electrolyte interfaces) in determining the overall performance of lithium-ion batteries has been appreciated for some time, and considerable effort has been devoted to investigating surface and interface phenomena with the aim of engineering more desirable traits.^{1–4} In general, crystal surfaces are inherently less stable (higher free energy) compared to the crystal bulk because of the different (distorted and truncated) coordination and chemical environments of the surface atoms. In addition, during synthesis and/or electrochemical cycling, oxygen can easily be lost from oxide crystals^{5–7} through their surfaces,^{7,8} affecting significantly the physical and

electrochemical performance of a host of materials.^{3–6,10–17} Capacity loss during high-voltage cycling of layered cathode material $\text{LiNi}_{0.4}\text{Mn}_{0.4}\text{Co}_{0.18}\text{Ti}_{0.02}\text{O}_2$, for example, has been attributed to deleterious surface reconstruction involving formation of oxygen-deficient (reduced) layers 1–2 nm thick.¹⁸

Recently there has been considerable interest in the role of oxygen loss during de- and re-intercalation of Li in Li-excess materials such as $\text{Li}_{1+x}\text{Mn}_{1-x}\text{O}_2$.^{19–21} To date, only a handful of studies have examined its role in the case of LiMn_2O_4 spinel, even though oxidation of the electrolyte during the charge-discharge process is known to produce a permeable surface layer with complex chemistry.²² As well as being of fundamental interest, these studies reiterate how the underlying mechanisms controlling oxygen loss from electrode materials need to be understood in order to design better electrode materials for long-life operation in high-power applications.

LiMn_2O_4 is an attractive cathode material owing to its low cost, non-toxicity, high rate capability and good safety performance.^{23–25} Stoichiometric LiMn_2O_4 has a cubic spinel crystal structure (space group $Fd\bar{3}m$) at ambient temperature, with Li atoms occupying 1/8th of the tetrahedral 8a sites and equal numbers of Mn^{3+} and Mn^{4+} atoms randomly distributed over half of the octahedral 16d sites (Fig. 1). It is generally believed that extraction of all Li ions from LiMn_2O_4 , by either electrochemical cycling or acid leaching, is accompanied by a large volume decrease which results in formation of a metastable λ -

^aNanostructures Research Laboratory, Japan Fine Ceramics Center, Nagoya 456-8587, Japan. E-mail: c_fisher@jfcc.or.jp

^bKey Laboratory of Polar Materials and Devices, East China Normal University, Shanghai 200062, China

^cBattery Materials Division, Toyota Motor Corporation, Susono, Shizuoka 410-1193, Japan

^dInstitute of Engineering Innovation, The University of Tokyo, Tokyo 113-8656, Japan. E-mail: ikuhara@sigma.t.u-tokyo.ac.jp

† Electronic supplementary information (ESI) available. See DOI: 10.1039/c8ta08083f

‡ Present address: Center for High Pressure Science and Technology Advanced Research (HPSTAR), Beijing 100094, China.

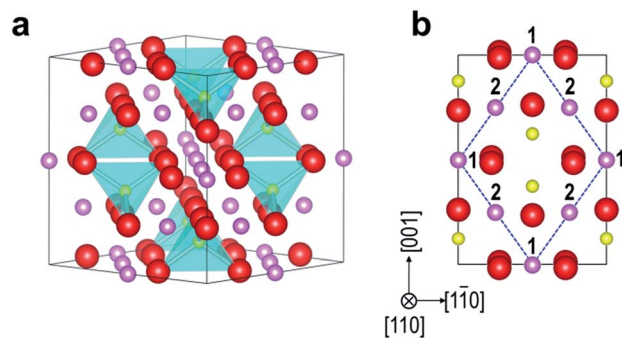


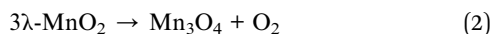
Fig. 1 (a) Unit cell of the LiMn_2O_4 spinel structure (space group $Fd\bar{3}m$) with Li (small yellow spheres at the centres of tetrahedra); Mn (mid-size magenta spheres); and O (large red spheres). (b) Projection of the unit cell along the (110) zone axis showing separate Li, Mn and O columns using the same atom representations as in (a). In the (110) projection there are two types of Mn columns arranged in a diamond-type configuration (dashed blue lines). Type 1 columns have twice the atom density as type 2 columns.

MnO_2 -like phase retaining the parent cubic structure.^{26–29} This delithiation process can be described by the equation



Lithium manganese spinels are also known to undergo dissolution of manganese in the form of Mn^{2+} ions from particle surfaces into non-aqueous liquid electrolytes upon electrochemical cycling.^{30–33} Manganese dissolution is widely believed to be an important factor behind the rapid capacity loss that has long hampered the commercialisation of these materials.³⁴ However, its underlying causes and means of prevention remain elusive.

Jang *et al.* reported that Mn dissolution is very high in the charged state, indicating that the rate of dissolution increases as Li content decreases,³⁵ and Hirayama *et al.* showed that dissolution rates also vary depending on the surface stability and hence surface orientation and structure.³⁶ More recently, based on scanning transmission electron microscopy (STEM) observations, Tang *et al.* traced the reason for Mn dissolution back to the instability of the delithiated phase, $\lambda\text{-MnO}_2$, which forms Mn_3O_4 on the surface upon release of oxygen:^{37,38}



One third of the cations in Mn_3O_4 are Mn^{2+} ions, so this phase is particularly susceptible to dissolution in acidic electrolytes.

In the above studies, LiMn_2O_4 surfaces were assumed to be fully stoichiometric when interpreting the results. However, it has been shown that LiMn_2O_4 particles contain a relatively high concentration of oxygen vacancies to a depth of about 10 nm from the surface in their as-prepared form.⁸ Notably, based on electrochemical measurements, Xia *et al.* found that oxygen off-stoichiometry was a key factor affecting the cycling performance of LiMn_2O_4 , particularly its capacity retention.¹⁵ These previous

studies all indicate that the dissolution and degradation mechanisms during electrochemical cycling of LiMn_2O_4 involve a complex interplay between Li content, Mn oxidation state, oxygen vacancy concentrations, interface structures and electrolyte chemistry.

The majority of studies of LiMn_2O_4 so far have relied on bulk analytical techniques such as X-ray/neutron diffraction and electrochemical measurements, which are unable to identify spatially localised structural and chemical changes at electrode surfaces, especially when the concentration of the small, weakly interacting Li atoms is low. Localised charge states and electron energy levels can be usefully probed using photoemission spectroscopies such as X-ray photoelectron spectroscopy (XPS) and ultraviolet photoelectron spectroscopy, but the spatial resolution is limited to several microns.³⁹ In the case of cathode materials, the observed behaviour may also depend on the particle size and morphology, the presence of conductive carbon additives, and the thickness of the solid electrolyte interface layer formed in contact with the liquid electrolyte (sometimes referred to as the cathode electrolyte interphase, or CEI), which itself is a function of the type of electrolyte used.^{36–41}

Recent advances in STEM techniques through the development of aberration correctors and monochromators have enabled materials to be probed with sub-ångstrom spatial resolution and high energy resolution so that complex interface structures (including surfaces) such as occur in Li-ion batteries can now be analysed at the atomic level.^{42–49} For example, Ben *et al.*⁵⁰ recently carried out a detailed study of changes in composition and structure of surfaces of LiMn_2O_4 nanoparticles using a combination of STEM, XPS and thermogravimetric/differential scanning calorimetry, showing that oxygen loss from the surface and the accompanying changes in charge state and distribution of Mn atoms correlate with loss of capacity. Dense thin films without coatings or additives are also well suited for such studies as their controlled morphologies facilitate systematic atomic-level observation of changes in the material's structure and properties as a function of battery charge state, particularly when prepared with high crystallinity and high epitaxy.

In this work we employ state-of-the-art STEM to probe atomic-level structural and compositional changes at surfaces of epitaxial LiMn_2O_4 thin films upon electrochemical extraction and insertion of Li ions during the first few cycles, as the initial cycles appear critical to the formation of stable cathode surfaces and CEIs.⁴¹ The $[110]$ projection of LiMn_2O_4 spinel is the most suitable for imaging as each column in this direction nominally contains only atoms of the same element (Fig. 1b); this crystal orientation was thus chosen for all direct structural observations in this work. The results provide further insights into the impact of surface structure degradation on the electrochemical performance of this important cathode material.

2. Experimental

2.1 Thin film deposition

A homogeneous metalorganic (Li–Mn–O) precursor solution was prepared by reacting $\text{LiOC}_2\text{H}_4\text{OC}_2\text{H}_5$ and $\text{Mn}(\text{OC}_2\text{H}_4\text{OC}_2\text{H}_5)_4$ in 2-ethoxyethanol, as described previously.³⁵ This solution

was used to prepare LiMn_2O_4 precursor films by spin coating onto clean $\text{Au}(111)/\text{Al}_2\text{O}_3(0001)$ substrates. The films were then transferred to a single-zone tube furnace and heated at $200\text{ }^\circ\text{C}$ for 30 min to remove the organic ligands, followed by further heating to $750\text{ }^\circ\text{C}$ for 1 h in oxygen. This sequence was repeated several times to obtain epitaxial LiMn_2O_4 films around 100 nm thick.

2.2 Electrochemical measurements

Electrochemical cells were constructed using an LiMn_2O_4 film as the cathode, Li metal as the anode, and propylene carbonate (PC) and 1 M LiClO_4 as the electrolytic solution. Each cell was assembled (and unloaded) in dry atmosphere in a glove box. Cyclic voltammetry (CV) measurements were performed with a scan rate of 0.1 mV s^{-1} between 3.0 and 4.5 V.

2.3 Microscopy

A 200 kV JEM-ARM (JEOL Ltd.) microscope equipped with a spherical-aberration corrector (CEOS GmbH) enabling structures to be probed with sub-ångström resolution was used for STEM imaging. A convergence angle of 25 mrad and annular dark-field detector inner/outer angles of 70/240 mrad and 29/70 mrad were chosen for HAADF and LAADF imaging, respectively. Electron energy-loss spectroscopy (EELS) was carried out using a JEM-ARM2400F (JEOL Ltd.) microscope equipped with a spherical-aberration corrector (CEOS GmbH), a Gatan Image Filter (GIF) and a Wien-filter type monochromator. An accelerating voltage of 120 kV, a convergence angle of 36 mrad and an energy resolution of 0.3 eV were selected for analyses of ionisation edges. Great care was taken to minimise exposure of the specimens to moisture and adverse electron beam irradiation effects. HAADF image simulation was carried out using the software package QSTEM.⁵¹ The Mn valence state was estimated using the white-line ratio (L_3/L_2) method reported by Varela *et al.*⁵² Details on how accurate Mn^{3+} concentration measurements were taken can be found in ref. 47.

Further details relating to thin film deposition, TEM specimen preparation and STEM-EELS analysis are provided as ESI.†

3. Results and discussion

LiMn_2O_4 thin films grown on $\text{Au}(111)/\text{Al}_2\text{O}_3(0001)$ substrates using a chemical deposition method were shown by XRD and TEM analyses to be epitaxial with an atomically abrupt and coherent interface between film and substrate, as reported previously.⁴⁷ The crystal orientation relationship can be written as $(111)_{\text{LiMn}_2\text{O}_4}/(111)_{\text{Au}}/(0001)_{\text{Al}_2\text{O}_3}$, $(110)_{\text{LiMn}_2\text{O}_4}/(110)_{\text{Au}}/(110)_{\text{Al}_2\text{O}_3}$. Film thicknesses varied between 50 and 100 nm both within and between samples. Films were subjected to charging and discharging over a number of cycles, and detailed STEM analysis of structure and composition near film surfaces was performed on samples of pristine (S0) and single-charged ($\text{S}^{1/2}$) films, as well as a film charged after four full cycles ($\text{S}^{4 1/2}$). The results are reported in the following sections.

3.1 Surface reconstruction during the first charge

3.1.1 Surface strain and compositional changes.

Whereas high-angle annular dark-field (HAADF) imaging allows positions of Mn columns to be determined with atomic resolution, low-angle annular dark-field (LAADF) imaging is capable of revealing strain fields and structural distortion from lattice mismatch or defects such as oxygen vacancies in crystalline oxides with high precision.^{42,47,53} Fig. 2a–d shows cross-sectional HAADF and LAADF STEM images taken from pristine (S0) and single-charged ($\text{S}^{1/2}$) samples. In the LAADF images, surface layers (arrowed in Fig. 2a and c) are substantially brighter than the crystal interior as a result of de-channelling of the incident electron beam caused by local distortions to the crystal lattice.^{54,55} Such brighter surface layers were not observed in the Z-contrast (where Z is atomic number) HAADF images taken from the same regions (Fig. 2b and d), indicating that there is substantial strain in the topmost crystal layers of both samples. Both the brightness and depth of this layer are greater in the case of sample $\text{S}^{1/2}$ than S0, indicating an increase in the magnitude and extent of the lattice distortion during the first charge.

Fig. 2e shows surface-to-bulk EELS intensity profiles of the Li K, O K, and Mn $L_{2,3}$ signals from samples S0 (filled) and $\text{S}^{1/2}$ (lines). In sample S0, Mn atoms are distributed more-or-less uniformly across the surface and bulk regions, while decreases in the Li K and O K intensities from bulk to surface reveal the existence of a surface layer (about 15 nm thick) deficient in these elements even before being placed in contact with the electrolyte. After extraction of Li (sample $\text{S}^{1/2}$), the intensity of the O signal in the surface layer (which broadens slightly to 20 nm) decreased slightly, while the Mn intensity

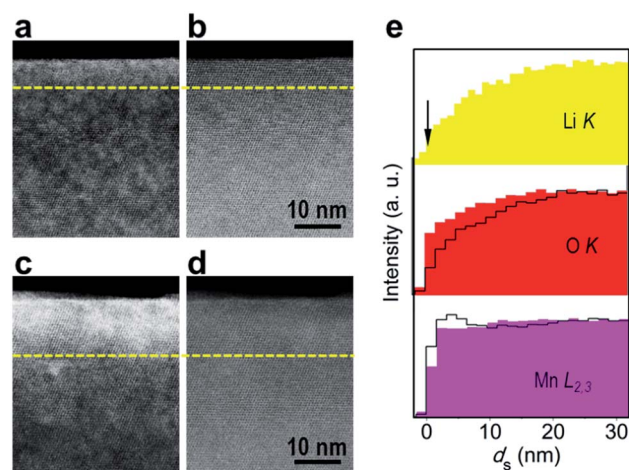


Fig. 2 Surface lattice distortion and element distributions. (a–d) Medium-magnification STEM images of LiMn_2O_4 epitaxial films down the [110] direction: (a) LAADF and (b) HAADF images of the same region of pristine (S0); (c) LAADF and (d) HAADF images of the same region of the first-charge half-cycle ($\text{S}^{1/2}$) sample. (e) Intensity-scan profiles of Li K, O K, and Mn $L_{2,3}$ electron energy-loss spectroscopy (EELS) signals obtained from samples S0 (filled) and $\text{S}^{1/2}$ (black lines), with the bulk-region intensities of O and Mn for $\text{S}^{1/2}$ roughly normalised to that of S0. The arrow in e indicates where the films terminate, *i.e.*, where the distance to the surface is 0.

increased in the topmost (≈ 5 nm) layer. These results indicate that additional loss of O accompanies Li removal, and the concentration of Mn atoms in the topmost layer increases during the first charge.

3.1.2 Structural phase changes. To obtain more detailed information about changes in surface structure, we performed high-resolution STEM imaging. Fig. 3a and b show cross-sectional HAADF images of the S0 (pristine) and S $\frac{1}{2}$ (single-charged) samples, respectively. In Z-contrast HAADF images, the bright Mn ($Z = 25$) columns can be readily distinguished (Mn1 columns are brighter than Mn2 columns because of their higher column densities), while the lighter O ($Z = 8$) and Li ($Z = 3$) columns are barely visible due to their weak scattering of electrons to high angles. In sample S0, the spinel structure

extends from the film bulk to the topmost surface layer, with an atomically abrupt surface terminated uniformly parallel to (111) $_{\text{LiMn}_2\text{O}_4}$ (seen more clearly in the magnified image on the right side of Fig. 3a). Note that {111} $_{\text{LiMn}_2\text{O}_4}$ surfaces are known to be the most thermodynamically stable in spinel LiMn $_2$ O $_4$, and dominate the morphologies of LiMn $_2$ O $_4$ particles.^{56–58} Such structural uniformity makes this film an excellent model for studying changes at surfaces with high resolution.

In sample S $\frac{1}{2}$, a different atom arrangement to that in the pristine sample was observed near the film surface (to a depth of 3 to 5 Mn-diamond units, *i.e.*, between 1.5 and 2.5 nm), with discernable contrast appearing at tetrahedral 8a positions (Fig. 3b). This contrast indicates the presence of Mn atoms on Li sites (Mn $_{\text{Li}}$ antisite defects). Such a configuration is consistent

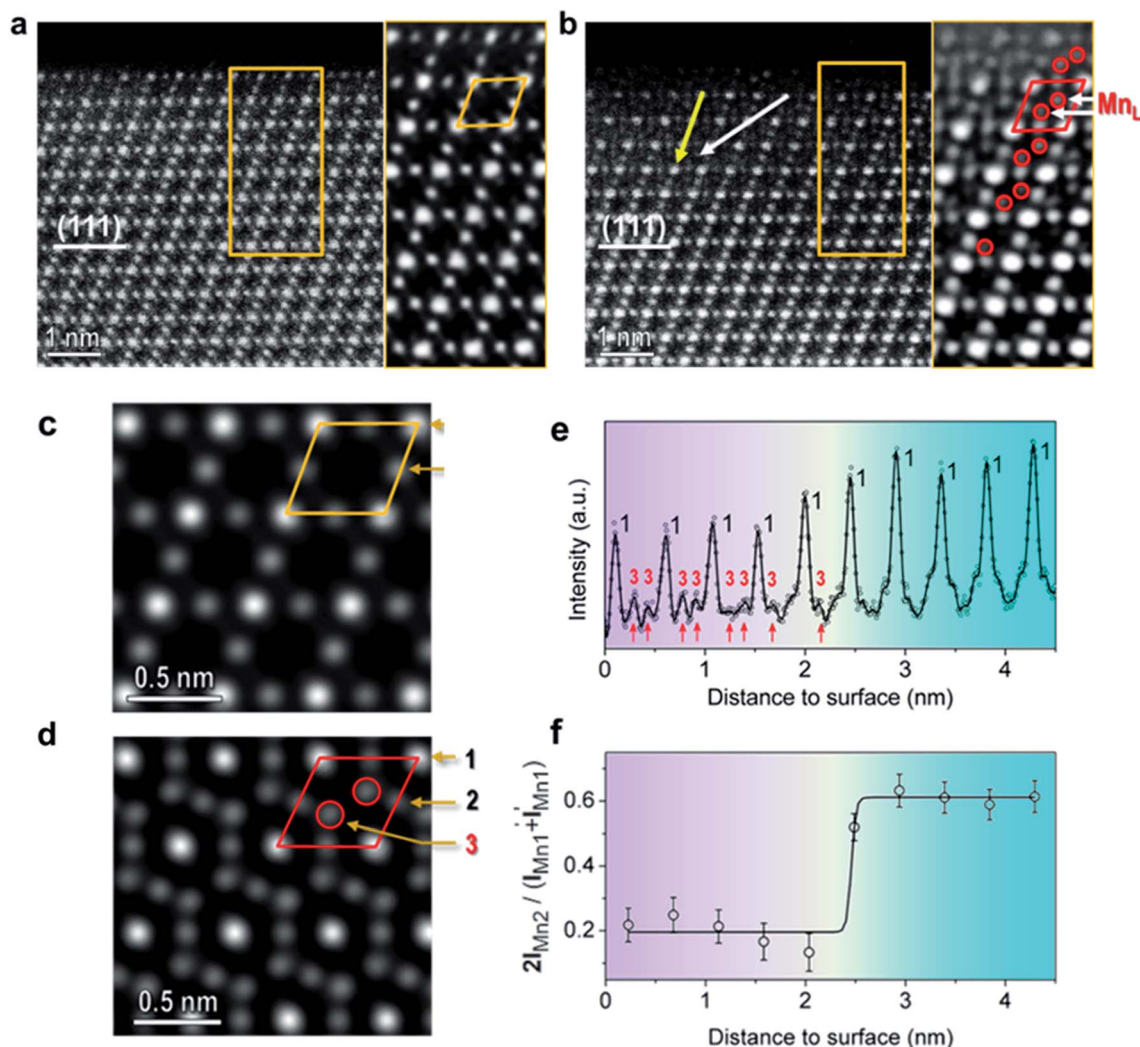


Fig. 3 Surface reconstruction during the first charge. High-resolution HAADF images revealing different atom configurations at (111) surfaces of (a) pristine (S0) and (b) first half-cycle (S $\frac{1}{2}$) LiMn $_2$ O $_4$ epitaxial films when viewed along [110]. The right panels in (a) and (b) show magnified noise-filtered HAADF images with Mn-diamond configurations highlighted to make the surface structure changes clearer. Simulated HAADF images show the arrangement of Mn atoms projected along (c) the [110] zone axis of LiMn $_2$ O $_4$ and (d) the [100] zone axis of Mn $_3$ O $_4$. The Mn1 (Mn $^{3+}$) columns in d have a linear atom density twice that of Mn2 (Mn $^{3+}$) or Mn3 (Mn $^{2+}$) columns. (e) Mn column intensity along an Mn1–Mn $_{\text{Li}}$ –Mn $_{\text{Li}}$ –Mn1 atom plane as a function of distance from the surface for sample S $\frac{1}{2}$. (f) Mn column intensity ratio $2I_{\text{Mn2}} / (I_{\text{Mn1}} + I'_{\text{Mn1}})$, where I_{Mn1} and I'_{Mn1} refer to the measured intensities of two Mn1 columns neighbouring an Mn2 column, down an Mn1–Mn2–Mn1 atom plane as a function of distance from the surface for sample S $\frac{1}{2}$. Planes of atom columns used in intensity-scan measurements in e and f are indicated in b as white and yellow arrows, respectively.

with the Mn_3O_4 structure projected along its (100) = (010) zone axis (Fig. S1 in ESI†), indicating that the LiMn_2O_4 surface layer has transformed to Mn_3O_4 during the first charge. This interpretation is supported by the excellent agreement between experimental HAADF images of surfaces in the two samples and simulated HAADF images of LiMn_2O_4 and Mn_3O_4 surfaces shown in Fig. 3c and d, respectively.

Fig. 3e shows a plot of column intensity as a function of distance from the surface of sample $\text{S}^{1/2}$ for the plane of atoms indicated by the white arrow in Fig. 3b. Mn1 peaks become weaker, and contrast appears on Li sites, indicating the presence of Mn_{Li} antisite defects, close to the surface. Fig. 3f shows a plot of the ratio between two times the intensity of each Mn2 column (I_{Mn2}) and the sum of the intensities of its adjacent Mn1 columns (I_{Mn1} and I'_{Mn1}) as a function of distance from the surface down the $-\text{Mn1}-\text{Mn2}-\text{Mn1}$ -plane of atoms (indicated by the yellow arrow in Fig. 3b). This plot reveals that there is a decrease in the atom density of Mn2 columns in the Mn_3O_4 -like surficial layer, which ideally should be half that of the Mn1 columns, similar to the spinel phase. These two results together suggest that Mn atoms have moved from octahedral Mn1 and Mn2 16d sites onto adjacent tetrahedral 8a sites to form Mn_{Li} antisite defects during the first charge, producing a row of $-\text{Mn1}-\text{Mn}_{\text{Li}}-\text{Mn}_{\text{Li}}-\text{Mn1}$ -columns, but with some vacancies remaining into which Li ions can re-intercalate.

As the increase in Mn3 intensities in Fig. 3e is not as great as the decrease in Mn2 intensities, it is possible that some Mn has been lost to the electrolyte as Mn^{2+} ions. Because Mn_3O_4 itself has a higher Mn concentration (approx. 44.5 atoms per nm^3) than LiMn_2O_4 (approx. 34.4 atoms per nm^3), even taking into account the loss of some Mn^{2+} ions through dissolution, the formation of an Mn_3O_4 -like phase in the reconstructed surface layer explains the observed changes in the O K and Mn $L_{2,3}$ intensity profiles of the two samples (Fig. 2e).

EELS analysis using an aberration-corrected and monochromated electron beam enabled us to probe the changes that occur near the surface of the LiMn_2O_4 film after delithiation in greater detail. Fig. 4 shows background-subtracted Mn $M_{2,3}$ (together with Li K), O K and Mn $L_{2,3}$ EELS profiles obtained from subsurface ($0 < d_s < 3$ nm, where d_s denotes distance from the film surface) and bulk ($d_s > 15$ nm) regions of S0 and $\text{S}^{1/2}$ samples. EELS spectra obtained from standard crystalline manganese oxides, which are in good agreement with the data reported by Kurata and Colliex,⁵⁹ are also included for comparison. In Fig. 4a, the change in Li K intensity in the subsurface and bulk regions of S0 matches the intensity-scan results well (Fig. 2e), while the Li K signal is hardly discernable in $\text{S}^{1/2}$, consistent with Li atoms being almost entirely removed during charging.

In Fig. 4b, the pre-peak intensity of the O K edge in the subsurface region is slightly less than that in the bulk region in S0. This is associated with a slight decrease in the average Mn valence state in the subsurface region relative to the reference Mn $L_{2,3}$ fine structures (Fig. 4c). In transition-metal (TM) oxides the pre-peak originates from hybridisation between O 2p and TM 3d levels,⁵² so the smaller magnitude of this peak indicates greater filling of Mn 3d orbitals, and hence less oxygen in the coordination shell of Mn. These differences, including a lower

Li concentration (*i.e.*, more Li vacancies) in the surface region, can best be explained by the presence of oxygen vacancies in the pristine material.

Quantitative analysis of Mn^{3+} concentrations was carried out using the white-line ratio method.^{43–46,52} For this, the concentration of Mn^{2+} was assumed to be zero in the top surface region ($d_s < 2.0$ nm), where the concentration of antisite Mn_{Li} atoms is high (Fig. 4b). The results in Fig. 5a reveal an average Mn valence state of approximately +3.3 in the surface region of S0, compared to +3.5 in the underlying bulk region (the latter matching the expected value for stoichiometric LiMn_2O_4). The EELS results thus show that there is a bulk-to-surface composition gradient in the pristine film, with decreasing concentrations of Li and O vacancies as well as a lower average valence for Mn (higher concentration of Mn^{3+} ions) to maintain local charge neutrality the closer to the surface termination.

Fig. 5b compares plots of the LAADF peak intensities and Mn^{3+} concentrations as a function of d_s for sample $\text{S}^{1/2}$. After a single charge, the Mn^{3+} concentration remains high in the outermost Mn_3O_4 surface layer, but drops markedly from approx. 73% ($d_s < 3.75$ nm) to about 10% in the interior ($\text{Li}_\eta\text{Mn}_2\text{O}_4$, $0 < \eta \ll 1$). During the charging process, the removal of one Li^+ ion from LiMn_2O_4 is accompanied by the oxidation of one Mn^{3+} ion to Mn^{4+} (eqn (1)). The larger drop in Mn^{3+} concentration in the film interior, which originally contained much more Li than the Li- and O-deficient surface region (Fig. 2e), of sample $\text{S}^{1/2}$ can be ascribed to the removal of more Li ions during the charging process. Whereas full removal of Li from stoichiometric LiMn_2O_4 produces a large volume decrease (theoretically up to around 7.7%),²⁹ the increase in the number of Mn^{3+} species near the surface of sample $\text{S}^{1/2}$ results in a sharp increase in lattice volume (inducing a compressive lattice strain) that varies linearly with distance up to the reconstructed Mn_3O_4 -like layer. This observation explains the large increase in brightness from the film interior to the film surface in the LAADF image (Fig. 5b). Interestingly, the LAADF contrast is a maximum at the interface between the Mn_3O_4 top layer and spinel intermediate layer. This suggests that there is a critical level of compressive lattice strain above which the spinel framework is no longer stable and structural reconstruction occurs to form Mn_3O_4 .

A critical level of lattice strain helps explain why the thin surficial layer or selvedge forms as Mn_3O_4 rather than MnO or Mn_2O_3 during the first half cycle. As mentioned above, delithiated LiMn_2O_4 , *i.e.*, $\lambda\text{-MnO}_2$, is thermodynamically unstable relative to Mn_3O_4 , MnO and Mn_2O_3 .^{60–63} Assuming a pseudo-cubic structure for all four phases, the phase transformation sequence $\lambda\text{-MnO}_2 \rightarrow \text{Mn}_3\text{O}_4 \rightarrow \text{MnO} \rightarrow \text{Mn}_2\text{O}_3$ produces lattice volume expansions, respectively, of about 21.7%, 32.6% and 61.2% (Fig. S2†). The forming of Mn_3O_4 as a surficial layer thus induces the smallest compressive lattice strain while remaining connected to the underlying $\lambda\text{-MnO}_2$ layers; unlike MnO and Mn_2O_3 , Mn_3O_4 has a spinel-type structure similar to $\lambda\text{-MnO}_2$ and so remains bonded coherently with it. In addition to the smaller volume change, the transition between them is likely to be kinetically more favourable, *i.e.*, with a smaller

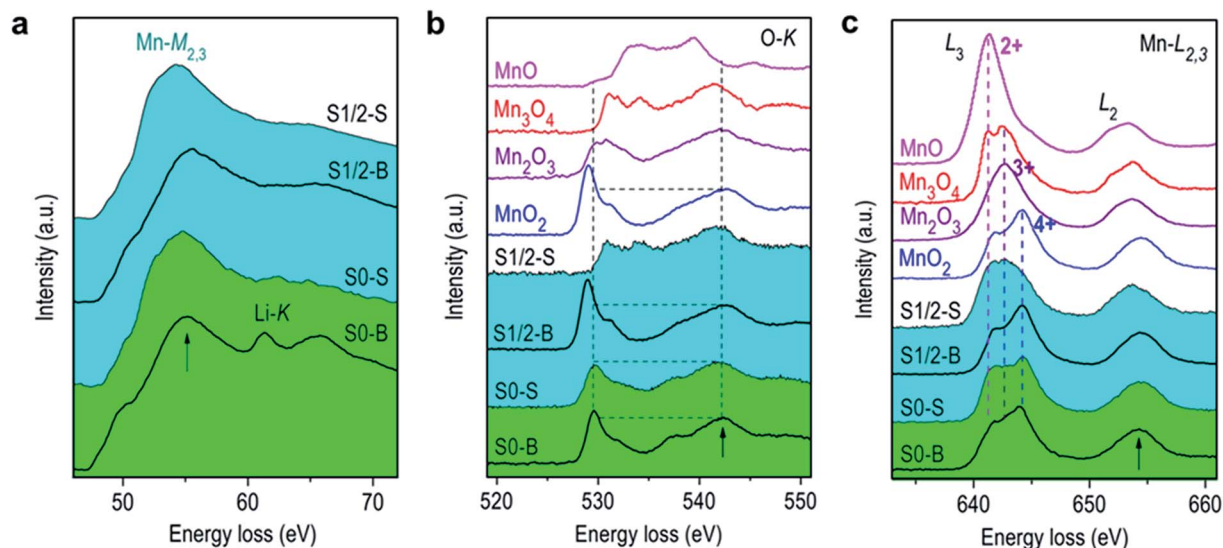


Fig. 4 Spatially-resolved electron energy-loss spectroscopy (EELS) analysis. (a–c) Background-subtracted spectra of (a) Mn $M_{2,3}$ (together with Li K), (b) O K, and (c) Mn $L_{2,3}$ edges, respectively, obtained from the surface and bulk regions of samples S0 (S0-S and S0-B, respectively) and $S^{1/2}$ ($S^{1/2}$ -S and $S^{1/2}$ -B, respectively), and from standard crystalline manganese oxides. Intensities of all profiles are normalised to those of the arrowed peaks. Suffixes S and B refer to surface and bulk regions, respectively.

transition energy barrier, because less rearranging of atom positions is required.

It has been reported previously that oxygen-deficient LiMn_2O_4 is thermodynamically unstable and decomposes to form tetragonal Mn_3O_4 at high temperatures.⁶ Similarly, we recently showed that a single unit-cell thick defective Mn_3O_4 layer forms at the interface between pristine LiMn_2O_4 epitaxial films and Au substrates due to oxygen deficiency and Jahn–Teller distortion induced by lattice mismatch.⁴⁶ A recent study by Amos *et al.* also found a thin surface layer of Mn_3O_4 on pristine LiMn_2O_4 particles.⁶⁴ These results suggest that Mn_3O_4 is stabilised by the compressive strain induced by lattice mismatch, and that the formation of Mn_3O_4 surface layers is an intrinsic feature of LiMn_2O_4 particles. Fig. 5b shows that further reduction of the surface layers through oxygen loss upon charging causes the width of the Mn_3O_4 region to increase from one lattice spacing to around six lattice spacings (3–4 nm), consistent with the loss of O and Li determined from EELS (Fig. 2e and 4b).

Summarising the above findings we can state that (1) in a pristine LiMn_2O_4 film, the narrow selvedge is subject to considerable compressive lattice strain because of inherent O and Li deficiency in the outermost crystal layers; (2) during electrochemical charging, the lattice strain in the O- and Li-deficient surface region increases markedly because of the drastic reduction in concentrations of Li^+ and Mn^{3+} ions, and hence lattice volume, in the subsurface and interior regions; (3) this strain is ameliorated in the selvedge by surface reconstruction whereby a coherently bonded surficial “ Mn_3O_4 -like” layer forms.

3.2 Effect of surface structure changes on Li-ion conductivity

Fig. 6a shows a HAADF image taken from the surface region of a film after one charge–discharge cycle, sample S1.

Interestingly, it was found that the surface region once again had the spinel structure, *i.e.*, the same structure as the film before cycling. Formation of an electrical double layer and CEI during the initial charge means that full re-oxidation of the surficial layer is thermodynamically unfavourable, so the return of a highly crystalline spinel layer at the surface can be best explained by removal of the surficial Mn_3O_4 during discharge, possibly by spalling as a result of the large stresses in the outermost layers observed using LAADF, as well as Mn^{2+} dissolution.⁶⁵ Upon repeated cycling, continued loss of O and Mn (according to eqn (2)) and removal of Li results in an increasingly defect-rich surface which compromises the integrity of the spinel framework so that a 1–2 nm thick MnO (rocksalt-type) top layer forms. Such a layer is shown in Fig. 6b for the sample after four and half cycles, $S^{1/2}$. Despite the different space group symmetries of the two phases (MnO and $\text{Li}_7\text{Mn}_2\text{O}_{4-y}$), the interface between the reconstructed surface and the spinel bulk remained coherent in these samples, suggesting that there is a structural gradient concomitant with the compositional gradient between the two phases that corresponds to a structural transition region of ~ 15 nm. As the MnO phase contains Mn^{2+} ions exclusively, further cycling can be expected to result in gradual loss of capacity through Mn^{2+} dissolution even after formation of the CEI, which may explain the capacity fading characteristic of LiMn_2O_4 spinel cathodes. To clarify the long-term degradation process, further STEM observations and accompanying electrochemical measurements will need to be performed on films subjected to tens or hundreds of cycles, which is beyond the scope of this work.

3.3 Electrochemical properties

As described in the previous sections, the thin defect-rich surface layers observed by STEM after charging are expected

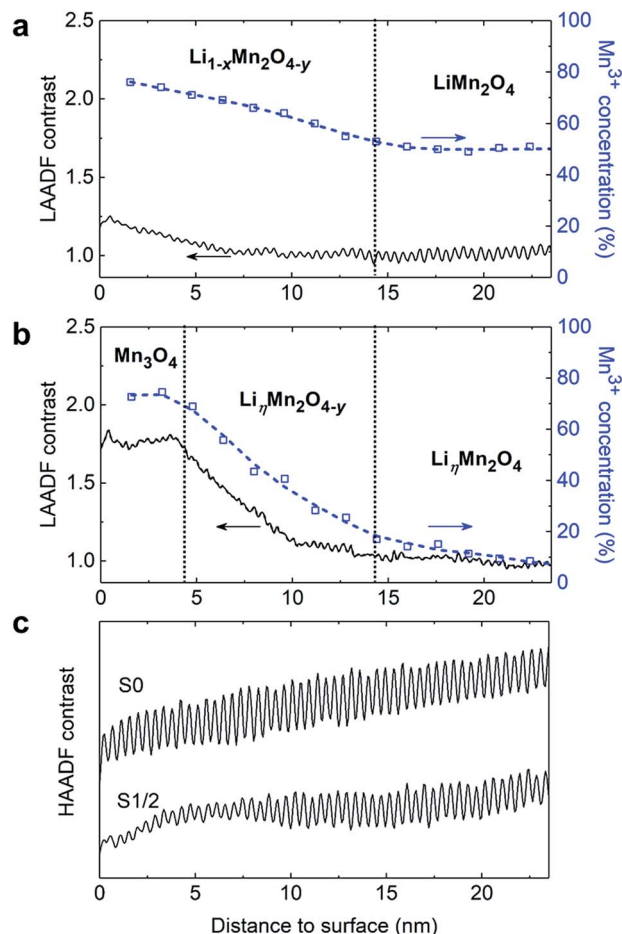


Fig. 5 Relationship between surface structure distortion and composition gradients in LiMn_2O_4 . (a and b) Profiles of normalised LAADF contrast and Mn^{3+} concentration as a function of distance to the surface (d_s) of (a) pristine (S0) and (b) first charge half-cycle (S_{1/2}) samples. (c) Integrated HAADF contrast profiles from Fig. 2b (S0, top) and 2d (S_{1/2}, bottom). The LAADF contrast profiles in (a) and (b) were obtained by normalising the integrated contrast in Fig. 2b and d, respectively, to the average intensity of their bulk regions, *i.e.*, the LiMn_2O_4 region in a and the $\text{Li}_\eta\text{Mn}_2\text{O}_4$ region in b, as demarcated by dotted lines. Vertical dashed lines indicate roughly the boundaries between different phases. Note that in $\text{Li}_{1-x}\text{Mn}_2\text{O}_{4-y}$, $\text{Li}_\eta\text{Mn}_2\text{O}_{4-\delta}$ and $\text{Li}_\eta\text{Mn}_2\text{O}_4$, $0 < x < 1$, $0 < y < 1$ and $0 < \eta \leq 1$.

to affect the cycle performance and capacity of the thin films because of their markedly different electrical properties compared to the bulk spinel phase. This interpretation is borne out by CV curves in Fig. 7.

Curves for the first and fourth cycles both exhibit two pairs of well-separated redox peaks at around 4.0 V and 4.13 V (curves for the second and third cycles were similar to those of the fourth cycle). These peaks are characteristic of lithium manganese spinels prepared as either powders or films, and indicate that the Li ions are extracted and inserted between LiMn_2O_4 and $\lambda\text{-MnO}_2$ in a two-step process.^{66–68} From the areas bounded by each curve, the capacity of the film is found to decrease by about 7.8% after four cycles. Similar to $\text{LiNi}_{0.4}\text{Mn}_{0.4}\text{Co}_{0.18}\text{Ti}_{0.02}\text{O}_2$,¹⁸ this decrease occurs predominantly during the first charge, with the initial specific charge capacity of 124 mA h g^{-1} falling to

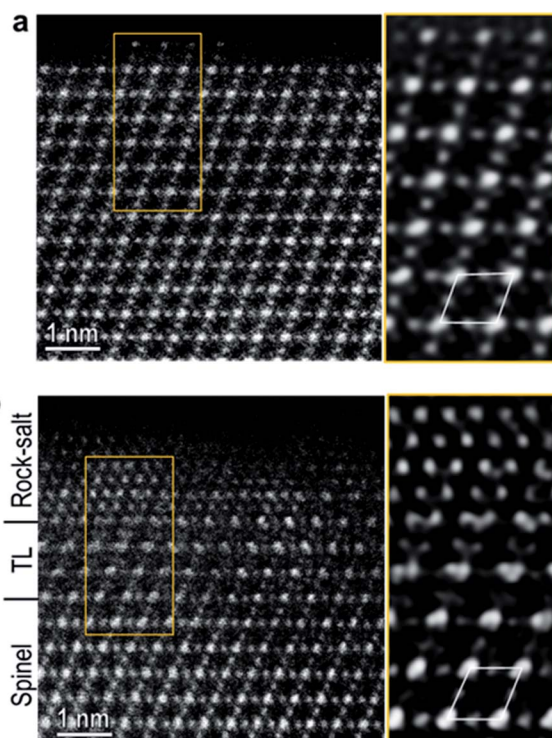


Fig. 6 Surface structure degradation upon repeated electrochemical cycling. HAADF images of LiMn_2O_4 films viewed along (110) showing positions of Mn atoms at surfaces after (a) one charge–discharge cycle (S1) and (b) four charge–discharge cycles and one charge half-cycle (S_{4 1/2}). Magnified filtered images of the regions in yellow rectangles in a and b, together with Mn–diamond configurations corresponding to the spinel network, are shown to the right of each image. Labels on the left side of b indicate the structure types of the adjacent regions (TL = transition layer).

106 mA h g^{-1} in subsequent charges; the discharge capacities fall to around 101 mA h g^{-1} in each case. The large drop in capacity ($\sim 15\%$) during the initial charge is consistent with loss of active material inferred from STEM micrographs such as that in Fig. 6a.

The gap between oxidising and reducing peaks in Fig. 7 can also be seen to narrow after the first cycle, indicating a decrease in polarisation at the electrode–electrolyte interface. This is accompanied by a slight increase in current during oxidation (charging) and decrease in current during reduction (discharging) during the fourth cycle, indicating Li ions are more easily removed than replaced after the interface has been “conditioned” through formation of an electrical double layer.⁴¹ Because rock salt-structured MnO impedes Li-ion diffusion, the increased current peaks, particularly that at lower voltage, suggest it forms towards the end of the charge half-cycle, *i.e.*, at high voltage, when the high concentration of vacant Li vacant sites become occupied by Mn^{2+} ions with further O loss from the surface.

During discharge, in contrast, MnO layers impede re-intercalation of Li, resulting in a lower specific capacity and smaller and broader current peaks. The rock-salt layer thus acts as a passivating layer, inhibiting rapid cycling of the half-cell. At

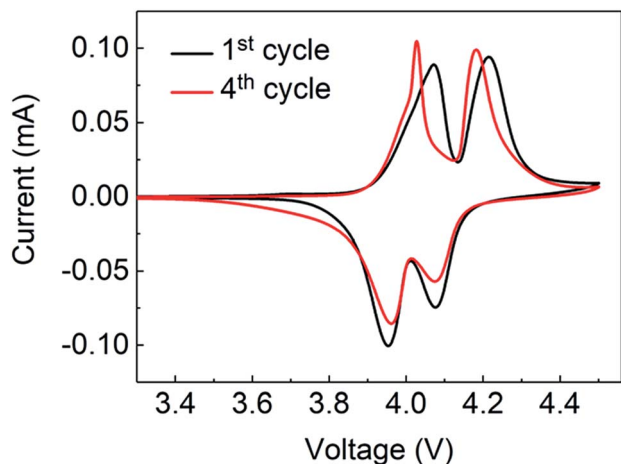


Fig. 7 Cyclic voltammetry (CV) curves for the first and fourth charge–discharge cycles of an LiMn_2O_4 thin film using a scan rate of 0.1 mV s^{-1} between 3.0 and 4.5 V. The area enclosed by the curves decreases about 7.8% between the two cycles, with the greatest decrease occurring during the first charge half-cycle.

the low cycle rate of 0.1C, however, the reduced rate of capacity loss after the first cycle suggests that the CEI has stabilised the surface structure or at least slowed down the rate of Mn^{2+} dissolution. The use of an epitaxial thin film with, in effect, a single surface exposed to the electrolyte may favour formation of this stable electrical double layer.

The above results reveal the important effect of oxygen loss and compositional and electrostatic gradients on the stability and chemical reactivity of surfaces of oxide electrode materials. The results are in good agreement with previous electrochemical studies, which have shown that the greater the oxygen deficiency in spinel lithium manganese cathode materials the poorer the capacity performance.^{9–13} Oxygen loss also depends on kinetic and mechanical factors such as cycling rate, voltage span, and applied pressure, so these are expected to have a strong influence on the rate of surface reconstruction and dissolution, and thus capacity loss, as well. Means of minimising surface reconstruction, for example, by minimising oxygen substoichiometry in as-prepared materials through appropriate choice of synthesis method, doping elements or coating layer, thus represent useful strategies for improving the cycling performance of LiMn_2O_4 -based cathodes.

Conclusions

In this study we examined structural and compositional changes at surfaces of LiMn_2O_4 epitaxial films at the atomic level by performing direct STEM (EELS) observations before, during and after the first few charge–discharge cycles, and correlated them with changes in electrochemical performance. The results show unambiguously that O deficiency near the surface of pristine LiMn_2O_4 is associated with Li deficiency and a mean oxidation state for Mn lower than expected from the canonical intercalation reaction. This non-stoichiometry produces a thin surface layer (whose approximate

composition of $\text{Li}_{1-x}\text{Mn}_2\text{O}_{4-y}$ varies gradually to a depth of $\sim 15 \text{ nm}$) that, although retaining a spinel-like framework coherently bonded to the crystal interior, is subject to considerable compressive lattice strain. The strain in the surficial layer increases significantly during the first charge as a result of the decrease in lattice volume inside the film when removal of Li causes Jahn–Teller Mn^{3+} ions to oxidise to smaller Mn^{4+} ions. The heavily strained surficial layer is unstable in this state, reconstructing to form Mn_3O_4 to a depth of 2–3 nm with further loss of oxygen; Mn^{2+} dissolution and/or spallation of the strained selvedge results in a large decrease in specific capacity during the first cycle.

Further electrochemical cycling was observed to result in further irreversible loss of oxygen and active material, as well as degradation of the surface structure, with rock-salt MnO forming as a selvedge phase after only a few cycles. The blocking of Li-migration pathways to the crystal bulk by what are in effect high concentrations of antisite cation defects at the surface, together with loss of active material through Mn^{2+} dissolution, helps explain the capacity fade characteristic of spinel cathode materials. This study demonstrates how atomic-resolution scanning transmission electron microscopy can be used to elucidate the impact of oxygen loss on surface structure and electrochemical performance of spinel-type lithium battery cathode materials at a fundamental level.

Conflicts of interest

There are no conflicts to declare.

Acknowledgements

Part of this research was supported by JSPS KAKENHI Grant Number JP26420693. The authors thank R. Yoshida at JFCC for help with TEM specimen preparation, and T. Hirayama and T. Kato at JFCC and Q. Zheng at Oak Ridge National Laboratory for helpful discussions.

References

- 1 J.-M. Tarascon and M. Armand, *Nature*, 2001, **414**, 359–367.
- 2 K. X. Wang, X. H. Li and J. S. Chen, *Adv. Mater.*, 2015, **27**, 527–545.
- 3 K. T. Lee, S. Jeong and J. Cho, *Acc. Chem. Res.*, 2012, **46**, 1161–1170.
- 4 J. Tarascon, W. McKinnon, F. Coowar, T. Bowmer, G. Amatucci and D. Guyomard, *J. Electrochem. Soc.*, 1994, **141**, 1421–1431.
- 5 R. Hausbrand, G. Cherkashinin, H. Ehrenberg, M. Gröting, K. Albe, C. Hess and W. Jaegermann, *J. Mater. Sci. Eng. B*, 2015, **192**, 3–25.
- 6 J. Sugiyama, T. Atsumi, T. Hioki, S. Noda and N. Kamegashira, *J. Alloys Compd.*, 1996, **235**, 163–169.
- 7 J. Sugiyama, T. Atsumi, A. Koiwai, T. Sasaki, T. Hioki, S. Noda and N. Kamegashira, *J. Phys.: Condens. Matter*, 1997, **9**, 1729–1741.

- 8 R. Huang, Y. H. Ikuhara, T. Mizoguchi, S. D. Findlay, A. Kuwabara, C. A. J. Fisher, H. Moriwake, H. Oki, T. Hirayama and Y. Ikuhara, *Angew. Chem., Int. Ed.*, 2011, **50**, 3053–3057.
- 9 M. Gu, A. Genc, I. Belharouak, D. Wang, K. Amine, S. Thevuthasan, D. R. Baer, J.-G. Zhang, N. D. Browning and J. Liu, *Chem. Mater.*, 2013, **25**, 2319–2326.
- 10 J. Song, D. W. Shin, Y. Lu, C. D. Amos, A. Manthiram and J. B. Goodenough, *Chem. Mater.*, 2012, **24**, 3101–3109.
- 11 P. V. Sushko, K. M. Rosso, J. G. Zhang, J. Liu and M. L. Sushko, *Adv. Funct. Mater.*, 2013, **23**, 5530–5535.
- 12 C. R. Fell, D. Qian, K. J. Carroll, M. Chi, J. L. Jones and Y. S. Meng, *Chem. Mater.*, 2013, **25**, 1621–1629.
- 13 X. Hao, X. Lin, W. Lu and B. M. Bartlett, *ACS Appl. Mater. Interfaces*, 2014, **6**, 10849–10857.
- 14 A. Naghash and J. Y. Lee, *J. Power Sources*, 2001, **102**, 68–73.
- 15 Y. Xia, T. Sakai, T. Fujieda, X. Yang, X. Sun, Z. Ma, J. McBreen and M. Yoshio, *J. Electrochem. Soc.*, 2001, **148**, A723–A729.
- 16 X. Wang, H. Nakamura and M. Yoshio, *J. Power Sources*, 2002, **110**, 19–26.
- 17 Y. Xia, H. Wang, Q. Zhang, H. Nakamura, H. Noguchi and M. Yoshio, *J. Power Sources*, 2007, **166**, 485–491.
- 18 F. Lin, I. M. Markus, D. Nordlund, T.-C. Weng, M. D. Asta, H. L. Xin and M. M. Doeff, *Nat. Commun.*, 2014, **5**, 3529.
- 19 K. Luo, M. R. Roberts, R. Hao, N. Guerrini, D. M. Pickup, Y.-S. Liu, K. Edström, J. Guo, A. V. Chadwick and L. C. Duda, *Nat. Chem.*, 2016, **8**, 684–691.
- 20 H. Chen and M. S. Islam, *Chem. Mater.*, 2016, **28**, 6656–6663.
- 21 D.-H. Seo, J. Lee, A. Urban, R. Malik, S. Kang and G. Ceder, *Nat. Chem.*, 2016, **8**, 692–697.
- 22 K. Edström, T. Gustafsson and J. O. Thomas, *Electrochim. Acta*, 2004, **50**, 397–403.
- 23 M. M. Thackeray, *Prog. Solid State Chem.*, 1997, **25**, 1–71.
- 24 O. K. Park, Y. Cho, S. Lee, H.-C. Yoo, H.-K. Song and J. Cho, *Energy Environ. Sci.*, 2011, **4**, 1621–1633.
- 25 B. Put, P. M. Vereecken, N. Labyedh, A. Sepulveda, C. Huyghebaert, I. P. Radu and A. Stesmans, *ACS Appl. Mater. Interfaces*, 2015, **7**, 22413–22420.
- 26 W. David, M. Thackeray, L. De Picciotto and J. Goodenough, *J. Solid State Chem.*, 1987, **67**, 316–323.
- 27 J. E. Greedan, N. Raju, A. Wills, C. Morin, S. Shaw and J. Reimers, *Chem. Mater.*, 1998, **10**, 3058–3067.
- 28 X. Yang, X. Sun, S. Lee, J. McBreen, S. Mukerjee, M. Daroux and X. Xing, *Electrochem. Solid-State Lett.*, 1999, **2**, 157–160.
- 29 A. Mosbah, A. Verbaere and M. Tournoux, *Mater. Res. Bull.*, 1983, **18**, 1375–1381.
- 30 W. Choi and A. Manthiram, *J. Electrochem. Soc.*, 2006, **153**, A1760–A1764.
- 31 R. Gummow, A. De Kock and M. Thackeray, *Solid State Ionics*, 1994, **69**, 59–67.
- 32 Y. Xia, Y. Zhou and M. Yoshio, *J. Electrochem. Soc.*, 1997, **144**, 2593–2600.
- 33 J. Park, J. H. Seo, G. Plett, W. Lu and A. M. Sastry, *Electrochem. Solid-State Lett.*, 2011, **14**, A14–A18.
- 34 A. Bhandari and J. Bhattacharya, *J. Electrochem. Soc.*, 2017, **164**, A106–A127.
- 35 D. H. Jang, Y. J. Shin and S. M. Oh, *J. Electrochem. Soc.*, 1996, **143**, 2204–2211.
- 36 M. Hirayama, H. Ido, K. Kim, W. Cho, K. Tamura, J. Mizuki and R. Kanno, *J. Am. Chem. Soc.*, 2010, **132**, 15268–15276.
- 37 D. Tang, L. Ben, Y. Sun, B. Chen, Z. Yang, L. Gu and X. Huang, *J. Mater. Chem. A*, 2014, **2**, 14519–14527.
- 38 D. Tang, Y. Sun, Z. Yang, L. Ben, L. Gu and X. Huang, *Chem. Mater.*, 2014, **26**, 3535–3543.
- 39 R. Hausbrand, D. Becker and W. Jaegermann, *Prog. Solid State Chem.*, 2014, **42**, 175–183.
- 40 C.-Y. Tang, K. Leung, R. T. Haasch and S. J. Dillon, *ACS Appl. Mater. Interfaces*, 2017, **9**, 33968–33978.
- 41 J. Cabana, B. J. Kwon and L. Hu, *Acc. Chem. Res.*, 2018, **51**, 299–308.
- 42 X. Gao, C. A. J. Fisher, T. Kimura, Y. H. Ikuhara, A. Kuwabara, H. Moriwake, H. Oki, T. Tojigamori, K. Kohama and Y. Ikuhara, *J. Mater. Chem. A*, 2014, **2**, 843–852.
- 43 X. Gao, C. A. J. Fisher, Y. H. Ikuhara, Y. Fujiwara, S. Kobayashi, H. Moriwake, A. Kuwabara, K. Hoshikawa, K. Kohama and H. Iba, *J. Mater. Chem. A*, 2015, **3**, 3351–3359.
- 44 L. Gu, C. Zhu, H. Li, Y. Yu, C. Li, S. Tsukimoto, J. Maier and Y. Ikuhara, *J. Am. Chem. Soc.*, 2011, **133**, 4661–4663.
- 45 C. Ma, K. Chen, C. Liang, C.-W. Nan, R. Ishikawa, K. More and M. Chi, *Energy Environ. Sci.*, 2014, **7**, 1638–1642.
- 46 X. Gao, S. Lee, J. Nichols, T. L. Meyer, T. Z. Ward, M. F. Chisholm and H. N. Lee, *Sci. Rep.*, 2016, **6**, 38168.
- 47 X. Gao, Y. H. Ikuhara, C. A. J. Fisher, H. Moriwake, A. Kuwabara, H. Oki, K. Kohama, R. Yoshida, R. Huang and Y. Ikuhara, *Adv. Mater. Interfaces*, 2014, **1**, 1400143.
- 48 Y. H. Ikuhara, X. Gao, R. Huang, C. A. J. Fisher, A. Kuwabara, H. Moriwake, K. Kohama and Y. Ikuhara, *J. Phys. Chem. C*, 2014, **118**, 19540–19547.
- 49 S. Kobayashi, C. A. J. Fisher, T. Kato, Y. Ukyo, T. Hirayama and Y. Ikuhara, *Nano Lett.*, 2016, **16**, 5409–5414.
- 50 L. Ben, H. Yu, B. Chen, Y. Chen, Y. Gong, X. Yang, L. Gu and X. Huang, *ACS Appl. Mater. Interfaces*, 2017, **9**, 35463–35475.
- 51 A. G. Dylla, G. Henkelman and K. J. Stevenson, *Acc. Chem. Res.*, 2013, **46**, 1104–1112.
- 52 M. Varela, M. Oxley, W. Luo, J. Tao, M. Watanabe, A. R. Lupini, S. Pantelides and S. Pennycook, *Phys. Rev. B: Condens. Matter Mater. Phys.*, 2009, **79**, 085117.
- 53 D. A. Muller, N. Nakagawa, A. Ohtomo, J. L. Grazul and H. Y. Hwang, *Nature*, 2004, **430**, 657–661.
- 54 S. Hillyard and J. Silcox, *Ultramicroscopy*, 1995, **58**, 6–17.
- 55 D. Perovic, C. Rossouw and A. Howie, *Ultramicroscopy*, 1993, **52**, 353–359.
- 56 T. Takada, H. Hayakawa, H. Enoki, E. Akiba, H. Slegel, I. Davidson and J. Murray, *J. Power Sources*, 1999, **81**, 505–509.
- 57 M.-R. Huang, C.-W. Lin and H.-Y. Lu, *Appl. Surf. Sci.*, 2001, **177**, 103–113.
- 58 A. Karim, S. Fosse and K. A. Persson, *Phys. Rev. B: Condens. Matter Mater. Phys.*, 2013, **87**, 075322.
- 59 H. Kurata and C. Colliex, *Phys. Rev. B: Condens. Matter Mater. Phys.*, 1993, **48**, 2102–2108.
- 60 A. Yamada and M. Tanaka, *Mater. Res. Bull.*, 1995, **30**, 715–721.

- 61 A. Yamada, K. Miura, K. Hinokuma and M. Tanaka, *J. Electrochem. Soc.*, 1995, **142**, 2149–2156.
- 62 A. Yamada, *J. Solid State Chem.*, 1996, **122**, 160–165.
- 63 J. C. Hunter, *J. Solid State Chem.*, 1981, **39**, 142–147.
- 64 C. D. Amos, M. A. Roldan, M. Varela, J. B. Goodenough and P. J. Ferreira, *Nano Lett.*, 2016, **16**, 2899–2906.
- 65 C. Zhan, J. Lu, A. J. Kropf, T. Wu, A. N. Jansen, Y.-K. Sun, X. Qiu and K. Amine, *Nat. Commun.*, 2013, **4**, 2437.
- 66 D. Aurbach, M. Levi, K. Gamulski, B. Markovsky, G. Salitra, E. Levi, U. Heider, L. Heider and R. Oesten, *J. Power Sources*, 1999, **81**, 472–479.
- 67 I. Yamada, T. Abe, Y. Iriyama and Z. Ogumi, *Electrochem. Commun.*, 2003, **5**, 502–505.
- 68 X. Hao, X. Lin, W. Lu and B. M. Bartlett, *ACS Appl. Mater. Interfaces*, 2014, **6**, 10849–10857.